Terminal Doppler Weather Radar Retrievals in Complex Terrain During a Summer High Ozone Period

Aaron C. McCutchan, John D. Horel, and Sebastian W. Hoch

University of Utah Department of Atmospheric Sciences, Salt Lake City, Utah

ABSTRACT: Observing boundary-layer winds in western US basins from NEXRAD WSR-88D radars is frequently hampered by the radars' locations at elevations far above basin floors. For example, KMTX in northern Utah is located 900 m above the Great Salt Lake and urban regions to the west of the Wasatch Mountains. Terminal Doppler Weather Radars (TDWRs) are located at several sites in the western US for wind shear detection near major airports. Radial distances to terrain obstructions vary substantially for TDWR scans as a function of elevation angle and azimuth. For example, low level scans toward the south from the TDWR located 20 km to the north of Salt Lake City International Airport (TSLC) are unobstructed to over 50 km, yet similar scans to the east are blocked at 6 km. Modifications were made to velocity volume processing and range-defined quasi-vertical profile retrievals to obtain vertical profiles of wind and reflectivity within a 5 km radius above TSLC. Idealized cases are used to illustrate the processing techniques. The methods are applied to the complex, diurnally varying flows observed within the boundary layer during 29 Aug - 7 Sep 2022 when northern Utah residents were exposed to exceptionally high ozone concentrations for that time of year.

SIGNIFICANCE STATEMENT: Residents in many urban basins of the western United States are exposed during summer to elevated ozone concentrations that contribute to substantial health impacts. Regional and local weather variations from summer-to-summer modulate the photochemical production of ozone. Northern Utah residents were exposed to unusually high ozone concentrations during 29 Aug - 7 Sep 2022. The complex, diurnally-varying boundary layer winds during this period are examined at high temporal and vertical resolution from radial wind observations obtained from the Terminal Doppler Weather Radar located near Salt Lake City International Airport.

1. Introduction

The depth and stability of the atmospheric boundary layer influences near-surface air pollutant concentrations and by extension public health (Hubbell et al. 2005; Fann et al. 2012; Sousa et al. 2013). After sunrise during summer, turbulent convective boundary layers (CBLs) often form in response to surface heating and deepen through the morning hours (Stull 1988). Biota (e.g. insects and birds) also become more active after sunrise, riding thermals within the turbulent CBL as it grows. During clear mornings, biota and Bragg scattering fill radar volumes, creating circles of elevated reflectivity around the radar.

Quasi-vertical profile (QVP) retrievals are used to create vertical profiles of scatterer properties by averaging radar moments observed along rings of constant range within a single conical scan and projecting them onto a vertical axis (Ryzhkov et al. 2016). Dual polarization antenna upgrades to the NEXRAD network have made it possible to differentiate between Bragg scattering and biota, further refining reflectivity based CBL depth estimates (Zrnic and Ryzhkov 1998; Bachmann and Zrnić 2007; Melnikov et al. 2011; Banghoff et al. 2018). Similar vertical profiles of horizontal wind fields can be estimated from radial velocity via velocity azimuth displays (VADs), a process fitting a sinusoid to radial velocity with respect to azimuth for rings of constant range (Browning and Wexler 1968; Doviak and Zrnic 1993; Teschke and Lehmann 2017).

VAD and QVP retrievals assume that conditions are homogeneous over large areas around the radar, which is rarely the case in regions of complex terrain. Additionally, many NEXRAD radars in the western US, such as KMTX near Salt Lake City, Utah (SLC), are intended to provide returns across mountainous terrain and are typically sited high above nearby low-lying areas with beam heights even further aloft. As a result, the NEXRAD network is often inadequate to observe CBL development in the western US using QVPs and VADs.

Terminal Doppler Weather Radars (TDWRs), a network of C-band single-pol Doppler radars, were installed beginning in 1994 to provide supplemental near-surface radar coverage around major airports prone to strong wind shear. The TDWR for SLC International Airport has been used to observe lake breezes from the Great Salt Lake (GSL), which have substantial implications for regional air pollution (Zumpfe and Horel 2007; Crosman and Horel 2016; Blaylock et al. 2017). Boundary layer development in this region is additionally complicated by thermally driven flows from the Wasatch and Oquirrh mountains, which carry their own impacts for air pollutant concentrations

Corresponding author: Aaron C. McCutchan, aaron.mccutchan@utah.edu

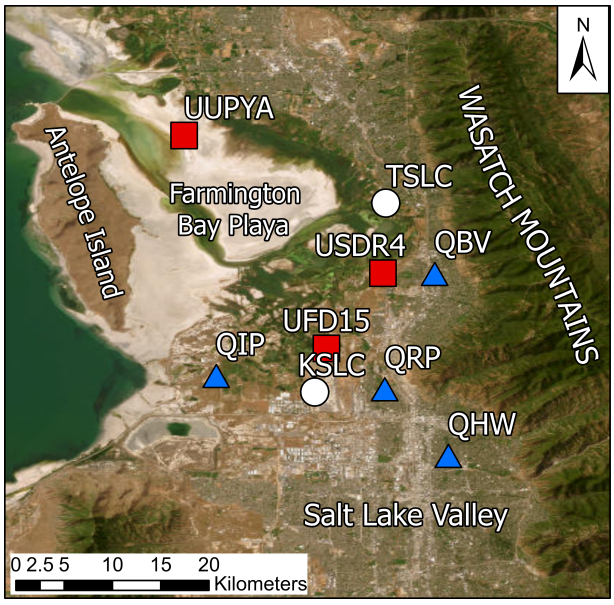

FIG. 1. Locations of key sensors for the 2022 summer ozone study and major geographic features of the Farmington Bay region. Blue triangles mark permanently installed Utah Division of Air Quality sensors. Red squares mark temporary Univeristy of Utah owned 2B Technologies ozone monitors, with additional meteorological equipment at UUPYA and UFD15. The white circles mark SLC International Airport (KSLC) with the radiosonde launch site and TSLC, the TDWR for the airport.

(Liu et al. 1992; Fast and Darby 2004; Jaffe 2011; Chow et al. 2013; Horel et al. 2016). The close proximity of urban SLC, GSL, and Wasatch mountains create unique opportunities to observe interactions between these flows and air pollution (Fig. 1).

The northern Wasatch front, containing the SLC metropolitan area and urban corridor to the north, is in moderate non-attainment of EPA National Ambient Air Quality Standards (NAAQS) for eight-hour average ozone ($\overline{O_3}$). To be in attainment, a location's daily max $\overline{O_3}$ cannot exceed 70 ppb more than three days over a rolling three year period. For simplicity in this study, we refer to any day where max $\overline{O_3}$ is over this limit as an exceedence day or event. The EPA has also proposed lowering the standard to 65 ppb, and we consider days with max $\overline{O_3}$ exceeding this threshold near-exceedance days or events.

In response to SLC's non-attainment status, the Utah Division of Air Quality (UDAQ) is responsible for writing a State Implementation Plan to be approved by the EPA outlining plans to mitigate hazards to the public and reduce concentrations. The University of Utah (UU) has been a key partner in advancing UDAQ's efforts to understand meteorological factors contributing to ozone pollution. A UU team in summer 2015 hypothesized that the Farmington Bay Playa (FBP), named after the arm of the GSL that used to fill the region to the east of Antelope Island, has significant influence upon ozone concentrations in the urban corridor between FBP and the Wasatch Mountains (Horel et al. 2016). Another UU team was funded to conduct a small field study during summer 2022 to investigate this hypothesis further (McCutchan 2023). The TDWR for SLC International Airport, TSLC, is located on the eastern portion of the study area, and was used during the 2015 study to monitor lake breezes (Blaylock et al. 2017). For the summer 2022 study, modified cousins of the VAD and QVP radar retrievals from TSLC provided high-value boundary layer observations in the form of time-height cross sections. Radar processing techniques developed for the summer 2022 study are the subject of this manuscript.

Section 2 gives an overview of boundary layer processes affecting ozone pollution in and around SLC. Section 3 gives an overview of modifications made to radar retrievals as well as data quality control steps applied, followed by a description of key datasets in section 4. Section 5 shows a composite of radar retrievals and ozone observations during a ten-day high ozone event, followed by a discussion of one day during the event where retrievals were particularly useful for characterizing boundary layer processes. McCutchan (2023) examined each day in the period in a similar manner. Section 6 summarizes and discusses these findings in a larger context while also suggesting directions for future work.

2. Wasatch Front Ozone

Ozone pollution is complex, developing due to a myriad of factors including precursor chemical concentrations, insolation, photochemical reactions, boundary layer processes, and transport by winds on all scales. While weather cannot be regulated, it does play a critical role in shaping the impacts of emissions. Thus, greater understanding of the impacts of atmospheric conditions on ozone concentrations may help development of effective regulations and mitigation strategies.

Along the Wasatch front, high ozone concentrations generally develop during dry, quiescent conditions. Ozone concentrations follow a diurnal cycle: they rise from a daily minimum at sunrise, reach peak near solar noon, decrease slowly through the late afternoon, decrease rapidly after sunset, and reach nighttime equilibrium near midnight local time.

Photochemical production is a major contributor to increases in ozone concentrations during the morning hours. Ozone is a secondary pollutant, created as a byproduct of volatile organic compounds (VOCs) being oxidized by nitrous oxides (NO_x) in the presence of sunlight, with both reactants sourced from urban emissions (Seinfeld and Pandis 2016). These reactions become more efficient at high ambient air temperatures (Pusede et al. 2015; Coates et al. 2016), thus ozone tends to be most problematic during summer heat waves. Ozone production is maximized at

solar noon due to the chemistry's dependence on incoming solar radiation (Baier et al. 2015). Overnight, these chemical processes reverse via titration (Seinfeld and Pandis 2016), deposition (Clifton et al. 2020), and halide scavenging (Simpson et al. 2007). Decreased titration from reduced NO_x and a lack of deposition lead to less reduction in ozone concentrations aloft, thus upon sunrise ozone concentrations tend to be lower at the surface than in layers aloft during quiescent conditions (Logan et al. 1981; Kaser et al. 2017).

When the sun rises, turbulent mixing within a shallow CBL under an inversion can act to increase ozone concentrations by bringing enhanced concentrations from aloft. Eventually, however, emissions trapped near the surface by the morning stable boundary layer lead to greater photochemical production, and ozone concentrations near the surface become greater than those aloft. In these situations, CBL growth entraining lower concentration air from aloft has a diluting effect, and is responsible for the slow decline in the afternoon (Kaser et al. 2017). The turbulent CBL leads to a deep mixed layer with uniform ozone concentrations by evening. After sunset, CBL turbulence wanes, radiative cooling dominates, and a stable boundary layer reforms near the surface.

Elevated ozone and precursor concentrations in the mid and upper troposphere contribute to increased $\overline{O_3}$ in many cities within the Intermountain West (Brodin et al. 2010). Downslope and down-valley winds transport background ozone aloft to basin floors at night (Liu et al. 1992; Jaffe 2011; Chow et al. 2013; Horel et al. 2016), while daytime upslope flows advect higher ozone concentrations from urban valleys up nearby slopes and canyons. Lake breezes also have significant influence upon ozone concentrations (Banta et al. 2011; Goldberg et al. 2014; Wentworth et al. 2015; Blaylock et al. 2017) and form in response to the greater thermal inertia of bodies of water such as the GSL. A similar yet weaker effect can happen over playa surfaces and wetlands such as FBP (Massey et al. 2017).

Figure 1 shows the major geographic features of the FBP and Salt Lake Valley (SLV) basins. During quiescent periods, mornings are often dominated by southerly flow over SLV and western FBP (Zumpfe and Horel 2007) along with an easterly jet that forms between the mouth of Weber Canyon and the northern side of Antelope Island (Chrust et al. 2013). Daytime heating reverses the thermally driven flows responsible, and flow becomes predominantly northerly. Both lake breezes and thermally-driven flows are most noticeable during quiescent periods, as both are easily overwhelmed by strong synoptic flow (Crosman and Horel 2010; Chow et al. 2013).

3. Radar Retrieval Methodology

Given an azimuth relative north α, elevation angle ϕ, and assuming scatterers are following the mean wind, Cartesian wind components are expected to yield a radial velocity value consistent with

$$V_r = u\ sin(\alpha)cos(\phi) + v\ cos(\alpha)cos(\phi) + w\ sin(\phi)$$

Theoretically, three sufficiently orthogonal radial velocities could be used to invert this relationship and resolve Cartesian wind components. In practice, turbulence and system noise in Doppler radars and lidars create too much variance for such methods to be stable (Teschke and Lehmann 2017; Wildmann et al. 2020). Instead, Fourier transforms or least squares regression with respect to azimuth along a ring of constant range are used to derive Cartesian wind components at a given height above the radar in the VAD retrieval (Browning and Wexler 1968; Doviak and Zrnic 1993). QVP retrievals average over other radar moments on the same rings of constant range to create a profile (Ryzhkov et al. 2016).

Such retrievals assume scatterers and the wind field remain uniform around the radar, often up to a radius of 50 km (Holleman 2005; Ryzhkov et al. 2016; Tobin and Kumjian 2017; Griffin et al. 2018; Hu and Ryzhkov 2022). Assuming such large uniform areas is unrealistic for radars in complex terrain. The size of the assumed uniform area can be reduced by scanning at a higher angle, decreasing vertical resolution, or only accepting a shallower profile. Effects of these tradeoffs can be reduced by combining conical scans at multiple elevation angles. Velocity Volume Processing (VVP) is one method to combine multiple elevation scans in a horizontal wind retrieval, and does so by allowing varying elevation in addition to azimuth in the least squares regression (Waldteufel and Corbin 1979; Boccippio 1995). A cylindrical domain centered on the radar is partitioned into stacked disks, and regression is carried out over gates within a given disk to create an estimate. In addition, statistics of other moments from gates within the disk can be calculated to form a vertical profile similar to a range-defined quasi-vertical profile (RD-QVP)(Tobin and Kumjian 2017).

For this study, we used a cylinder radius of 5 km, roughly the distance from TSLC to the nearest foothills. Disks were partitioned on a logarithmic axis, with the lowest disk being 3 m deep, and depths reaching up to 200 m aloft. Validation of the retrievals at TSLC using radiosondes from KSLC was undertaken, however local terrain often causes flow patterns between the two locations to differ considerably. Instead, accuracy of retrievals using this geometry were assessed using artificial wind fields. One set of results is presented in figure 2.

The wind field shown in figure 2a is composed of pure westerly flow from the surface to 1500 m and pure southerly flow 1500 m - 3000 m. Wind speeds start at 2.5 $m\ s^{-1}$ and increase to 5 $m\ s^{-1}$ between 500 m - 1000 m and 2000 m - 2500 m. Radial velocities from the specified wind field were generated using the above equation for each

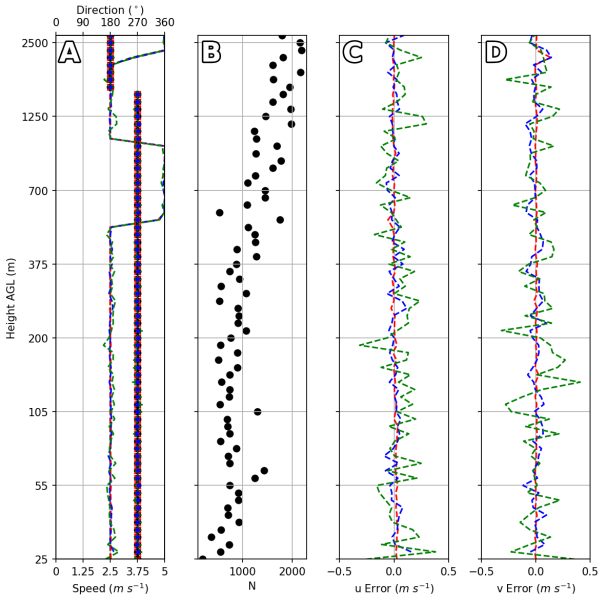

FIG. 2. Example of a VVP test using study retrieval geometry. Red series indicates retrieval when computed radial velocities are rounded to the nearest 0.5 $m\ s^{-1}$, blue indicates results when white noise with a standard deviation of 1 $m\ s^{-1}$ is applied before rounding, and green indicates results when white noise standard deviation is 5 $m\ s^{-1}$. (a) Profile used for testing and retrieval recreation on a logarithmic height axis. Black series indicates expected results. Line indicates wind speed ($m\ s^{-1}$), while scatter indicates wind direction (degrees). (b) Number of gates included in retrieval disks. (c) Zonal component error ($m\ s^{-1}$). (d) As in (c) for meridional component.

azimuth-elevation pair in TSLC's scanning geometry that falls within the sampling cylinder. After those calculations, white noise is added to the calculated radial velocities to simulate observational error and turbulence. Low amplitude noise had a standard deviation of 1 $m\ s^{-1}$, and high amplitude noise had a standard deviation of 5 $m\ s^{-1}$. The data were then rounded to the nearest 0.5 $m\ s^{-1}$ to mimic data resolution available in level 2 radar archives. Figures 2c and 2d show the error in zonal and meridional wind components, respectively. Figure 2b shows the number of gates incorporated into regression within a particular disk. Half of the available gates were rejected to simulate the effect of sparse scatterers and moment filtering as described later in this section.

The retrieval performed well, even for noisy data. Sudden wind field changes are used instead of gradual changes because sudden wind changes are more likely to create substantial error and used here to mark boundary layer features during case studies. Large depths of uniform wind speed allows assessment for changing bias with height and retrieval bin size. The errors never exceed 0.3 $m\ s^{-1}$ in either component for either series, nor does it show height dependency. The disk partitioning is well matched with the scanning geometry, roughly equally distributing gates between disks. The number of gates does increase with height, but in observed data lower scatterer counts are available away from the surface and fewer gates would be expected to contain data, offsetting the effect.

Prior VVP studies regressed over mean and first order terms of each wind component to create their estimates, but found that including higher order terms, when unimportant, reduced retrieval accuracy and retrieval stability (Waldteufel and Corbin 1979; Boccippio 1995; Shenghui et al. 2014). Artificial tests in this study showed that neglecting the vertical wind and higher order terms did not have significant impact on mean horizontal component retrieval accuracy within realistic values for unresolved terms. Thus, we chose to use only mean horizontal wind terms to maximize retrieval accuracy and stability.

Quality of data fed into the retrieval was also assessed. First, moment filters were applied, requiring reflectivity between -20 dBZ and 30 dBZ and spectrum width between 0.5 $m\ s^{-1}$ and 2 $m\ s^{-1}$. Filtering eliminates areas of significant precipitation and some vehicle traffic. Second, velocity data had to be non-zero, eliminating both weak returns and terrain blockage. Next, an outlier rejection filter is applied twice to the data (Pichugina et al. 2019; Banta et al. 2020). After this process was completed, the retrieval is run if more than 100 valid gates remain in the disk.

4. Datasets

a. TDWR Radar Network

TSLC is located on the east side of FBP (Fig. 1) and part of the larger TDWR network operated by the Federal Aviation Administration. Table 1 provides a comparison of TDWR and WSR-88D specifications. Data from both networks are archived publicly as part of the NOAA Open Data Dissemination Program (NOAA Information Technology 2023), with level-2 data from TSLC available Sep 2020 - present. Since TSLC is single-pol and KMTX only scans far above the basin floor, dual-pol products used by Banghoff et al. (2018) are unavailable. The volume coverage pattern (VCP) for TSLC is determined automatically, switching to hazard mode upon detection of meteorological echoes greater than 20 dBZ or wind shear near the airport (NOAA NCEI 2023b). In clear air mode, TSLC scans up to 60° elevation, considerably deeper than any VCP used by a WSR-88D, and was in this mode for most of the time in case studies presented later. TDWR dealiasing is handled at the data acquisition unit before transmission to end users using a multi-PRI method (Cho 2005, 2010). Since winds during the case studies stayed below the lowest possible TDWR aliasing velocity of 10 $m\ s^{-1}$, only rejected non-meteorological echoes are subject to aliasing.

Characteristic	TDWR	NEXRAD
Wavelength (cm)	5 (C-Band)	10 (S-Band)
Antenna Polarization(s)	Horizontal Only	Dual-Pol
Gate Length	150 m	250 m
Unambiguous Range	90 km	230 km
Clear Air Mode Scan Time	6 min	12 min
Hazard Mode Scan Time	3 min	4 min
Aliasing velocity	10 - 15 $m\ s^{-1}$	32 $m\ s^{-1}$
Beamwidth	0.5°	1.25°

TABLE 1. Operating characteristics of Next Generation Weather Radar (NEXRAD) and Terminal Doppler Weather Radar (TDWR) network radars (NOAA NCEI 2023a,b). Scan update times are approximate.

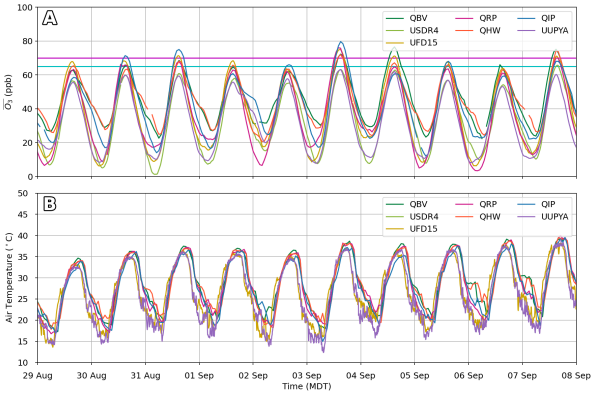

FIG. 3. Surface station observations from study sites during the LDP. (a) Timeseries of $\overline{O_3}$ (ppb). $\overline{O_3}$ values are computed from hourly (5 min) observations at UDAQ (UU) sites, respectively. Magenta line indicates present 70 ppb NAAQS $\overline{O_3}$ standard, and cyan line indicates proposed 65 ppb standard. (b) As in (a) except for air temperature (C°) at hourly (5 min) intervals at UDAQ (UU) sites, respectively.

b. Summer 2022 Ozone Study

The 2022 summer ozone study conducted by a UU team investigated the influence of FBP on ozone concentrations along the Wasatch Front using a network of surface observations and surface based remote sensors (McCutchan 2023). UDAQ has a number of permanently installed regulatory grade ozone monitors around the SLV and FBP basins (Fig. 1). Research grade 2B Technologies ozone monitors were placed at UUPYA, USDR4, and UFD15. Tower mounted meteorological sensors including wind and temperature were available at UUPYA and UFD15. USDR4 and UFD15 were set up along the edge of FBP to monitor transport near the region while UUPYA monitors conditions on the playa. Ozone reported at UDAQ sites are analyzed using one-hour averages. For comparison, a one-hour running mean smoother was applied to ozone concentrations reported every 5 minutes at UU sites.

5. 2022 Labor Day Period

A strong heat wave occurred in northern Utah 29 August 2022 - 13 September 2022. This period contained a large share of exceedance events observed during the summer ozone study (McCutchan 2023). Here we discuss 29 Aug 2022 - 7 Sep 2022, referred to as the Labor Day period (LDP) due to the observance of Labor Day on 5 Sep 2022. In this ten-day period, there were five $\overline{O_3}$ exceedance events and every day was at least a near-exceedance event (Fig. 3). Record high temperature and ozone events also occurred 9 - 12 Sep, however a synoptic disturbance transported wildfire smoke into the region. We exclude these days to focus on clear-sky conditions.

Synoptic conditions during the LDP were quite similar between each day and matched what is often observed during other quiescent periods. Shortwave radiation time series from UUPYA indicate the basin lacked significant cloud cover except during short periods during the mornings of 30 Aug and 1 Sep (not shown). Near-surface conditions from KSLC routine soundings were generally what is expected during weakly-forced situations. Potential temperature from the morning sounding on 6 Sep (Fig. 4) showed strong stability near the surface due to nocturnal radiative cooling, topped by a weakly stable layer. The evening sounding shows the stable layer eroded over the course of the day in response to radiative heating, becoming superadiabatic near the surface and creating a deep CBL. Similar profiles were observed every day during the LDP.

Figure 5 shows a composite of key datasets during the LDP. Figure 5a presents one-hour average ozone (O_3) and figure 5b shows one hour average ozone time rates of change (O_3') computed for seven sites. Composites for UDAQ sites were created by averaging the hourly observations across all days. Composites for UU sites were created using the one-hour average for the same hour as UDAQ observations. O_3' was calculated from the hourly data for UDAQ sites and smoothed data for UU sites then had the same averaging applied.

The mean of all seven sites (black solid line) show common features:

- O_3 minima near sunrise (0600 - 0700 MDT);
- Increase until after solar noon (1400 MDT);
- Slow decrease in the afternoon that becomes faster over time;
- Ozone values reach low equilibrium around midnight;
- Mostly constant O_3 in the early morning hours.

O_3 time series for individual sites tend to fall into one of two clusters overnight: a below average group containing

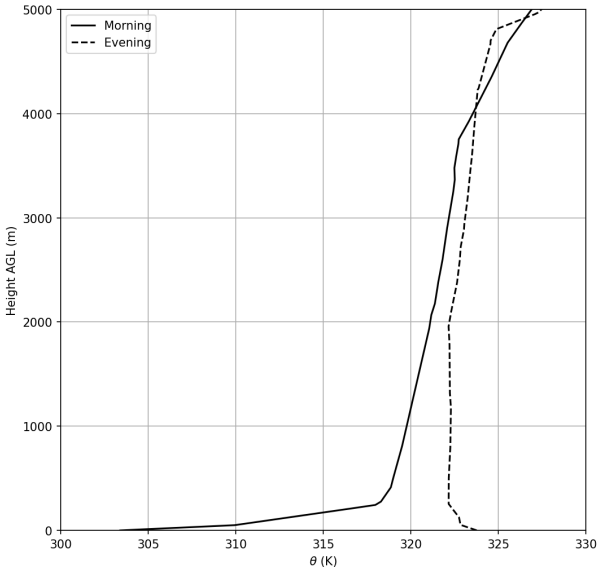

FIG. 4. Potential temperature (K) profiles derived from KSLC soundings on 6 Sep. Solid line indicates profile during the morning (12 UTC/06 MDT) sounding, and dashed line indicates profile from evening (00 UTC/18 MDT) sounding.

sites close to FBP (USDR4, UFD15, UUPYA) and a high urban cluster (QBV, QHW). QIP and QRP exhibit a mix of these two signals, reflecting their siting closer to the main body of the GSL and northern SLV urban area, respectively. In the morning, UFD15 tends to have higher than average O_3 and overall greatest daily swing, while UUPYA and USDR4 consistently have lower O_3.

Composite VVP winds for the LDP are shown in figure 5c. VVPs were averaged in height along the native logarithmic axis and time bins of 18 minutes, corresponding to roughly 3 volume scans. Zonal and meridional wind components were averaged to derive composite direction while wind speed was averaged separately.

At 0630 MDT, near the time of sunrise, flow near the surface switches from westerly to southerly, dissipating by 0700 MDT. Flow above 200 m goes through a similar transition, persists, and becomes southeasterly. At 0800 MDT, flow near the surface reappears, this time being northeasterly, and veers with height to become easterly. At 1000 MDT, near surface flow reverses, transitioning from northeasterly to northwesterly. Meanwhile, flow aloft increases and shifts from southeasterly to southerly.

Between 1100 - 1300 MDT, flow near the surface becomes westerly, and the height of the interface between westerly surface flow and southerly flow aloft marking the CBL top increases. By 1300 MDT, the CBL has grown beyond profile depth and this interface is no longer visible. Flow then becomes uniform, faster, and northwesterly through the entire profile beginning at 1400 MDT, likely in response to deep momentum transport within the CBL. Near sunset (2000 MDT), flow through the depth of the profile shifts from northwesterly to northeasterly and becomes decoupled from the surface. This northwesterly flow dissipates from the bottom up overnight, fully dissipating by 0300 MDT. Meanwhile, at 2230 MDT, weak southerly flow develops in a layer near the surface and persists with the northeasterly flow, becoming westerly at 0300 MDT until sunrise at 0600 MDT.

Composite mean reflectivity RD-QVPs (Fig. 5d) created using the same method show similar dependence upon boundary layer growth as noted in prior literature. Beginning at 0800 MDT, an area of increased reflectivity appears at the surface, deepening in step with boundary layer flow seen in the VVP. It reaches its peak depth at 1000 MDT, when the flow reversal occurs, then slowly decreases through the afternoon hours as scatterers are dispersed through the deepening boundary layer. Reflectivity then increases twice in the evening, the first due to bird activity near the radar and the second due to solar effects. A similar increase in reflectivity happens near 0630 MDT corresponding with sunrise.

While synoptic conditions were fairly similar through the LDP, subtle differences were present in the vertical wind profile each day. On 6 Sep, easterly flow aloft was stronger and more persistent than the composite (Fig. 6c). Easterly flow in this region corresponds to downslope flow, which typically displaces high ozone concentrations from the prior day's CBL and replaces them with lower background ozone concentrations overnight. As the CBL grows during the following day, decreased ozone concentrations aloft increase the diluting effect of CBL growth. Despite being one of the warmest days of the period, 6 Sep had some of the lowest observed $\overline{O_3}$ (Fig. 3). This enhanced easterly flow may indicate increased clearing of the RL by downslope flow, lowering surface ozone as the CBL grew in turn. The enhanced dilution effect can also be seen in the O_3' observations, where O_3' was lower than average during the morning hours and more negative during the afternoon compared to composite (Fig. 6b). Persistent easterly flow and reduced ozone concentrations (Fig. 3) were also seen on 5 Sep (not shown).

6. Discussion and Summary

Clear air returns from weather radars can be used to derive boundary layer wind fields at high temporal and vertical resolution. QVPs and VADs can be used to construct vertical profiles of radar moments and horizontal winds above the radar, but assume the area above the radar to be uniform. In complex terrain, areas meeting this assumption are limited in size, thus retrievals from a single conical scan must be rejected at a lower height. By combining multiple conical scans, retrieval vertical resolution and maximum depth can be improved.

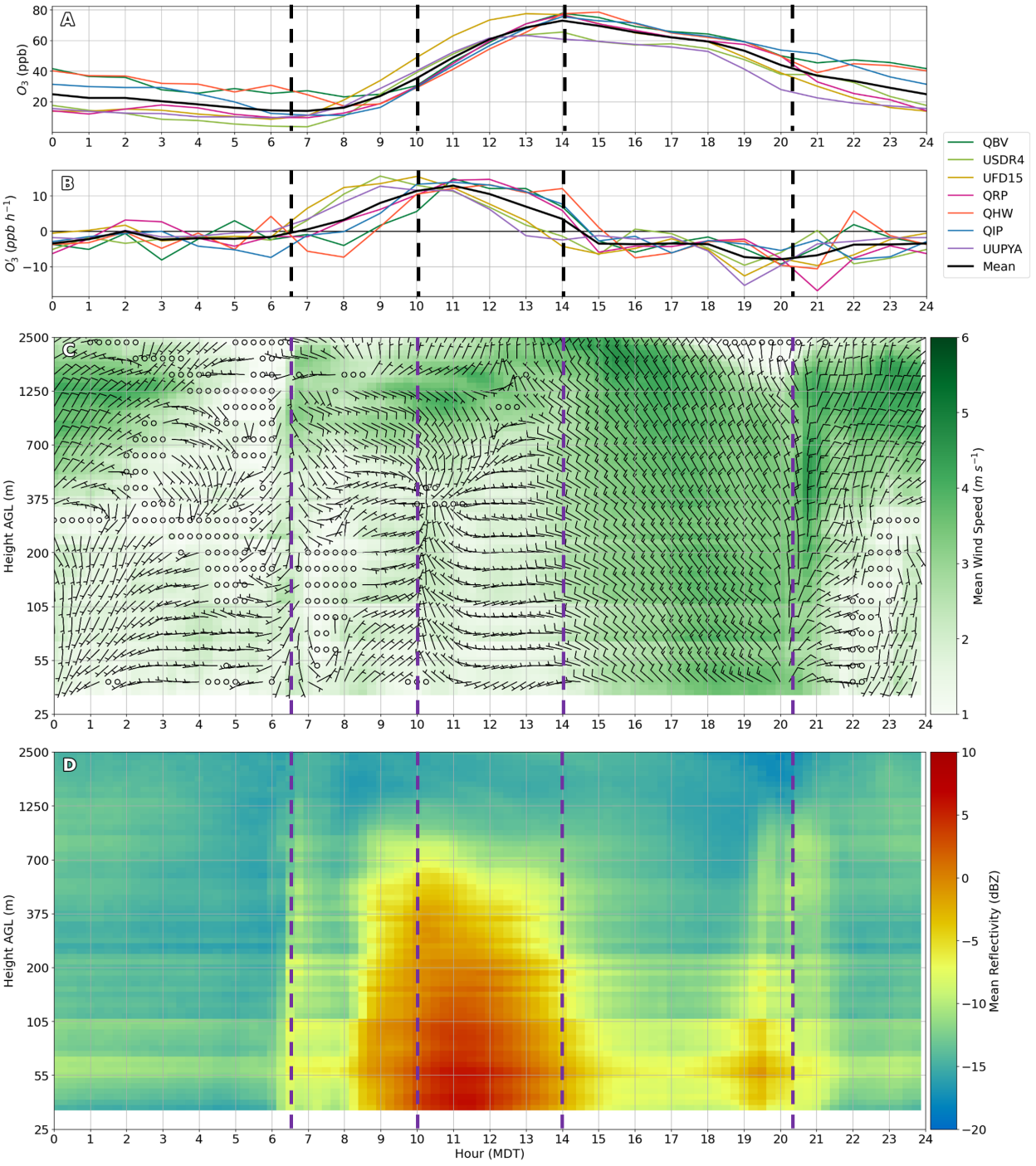

FIG. 5. Composite of observations made during the ten-day LDP. (a) Composite O_3 (ppb) computed within the LDP of UDAQ observations during each hour and hourly running mean observations at UU sites. (b) As in (a) except for O_3' (c) Composite TSLC VVP computed over native logarithmic height axis and 18 minute intervals (shaded, $m\ s^{-1}$) and wind barbs during the LDP. Half (full) barbs correspond to 1.25 (2.5) $m\ s^{-1}$. Every third barb in height is plotted.(d) As in (c) except for composite TSLC mean reflectivity RD-QVP (dBZ).

This study applied an under-utilized resource to examine the boundary layer: output from the TSLC TDWR. This single-pol radar is located close to the basin floor and samples in higher spatial and temporal resolution than

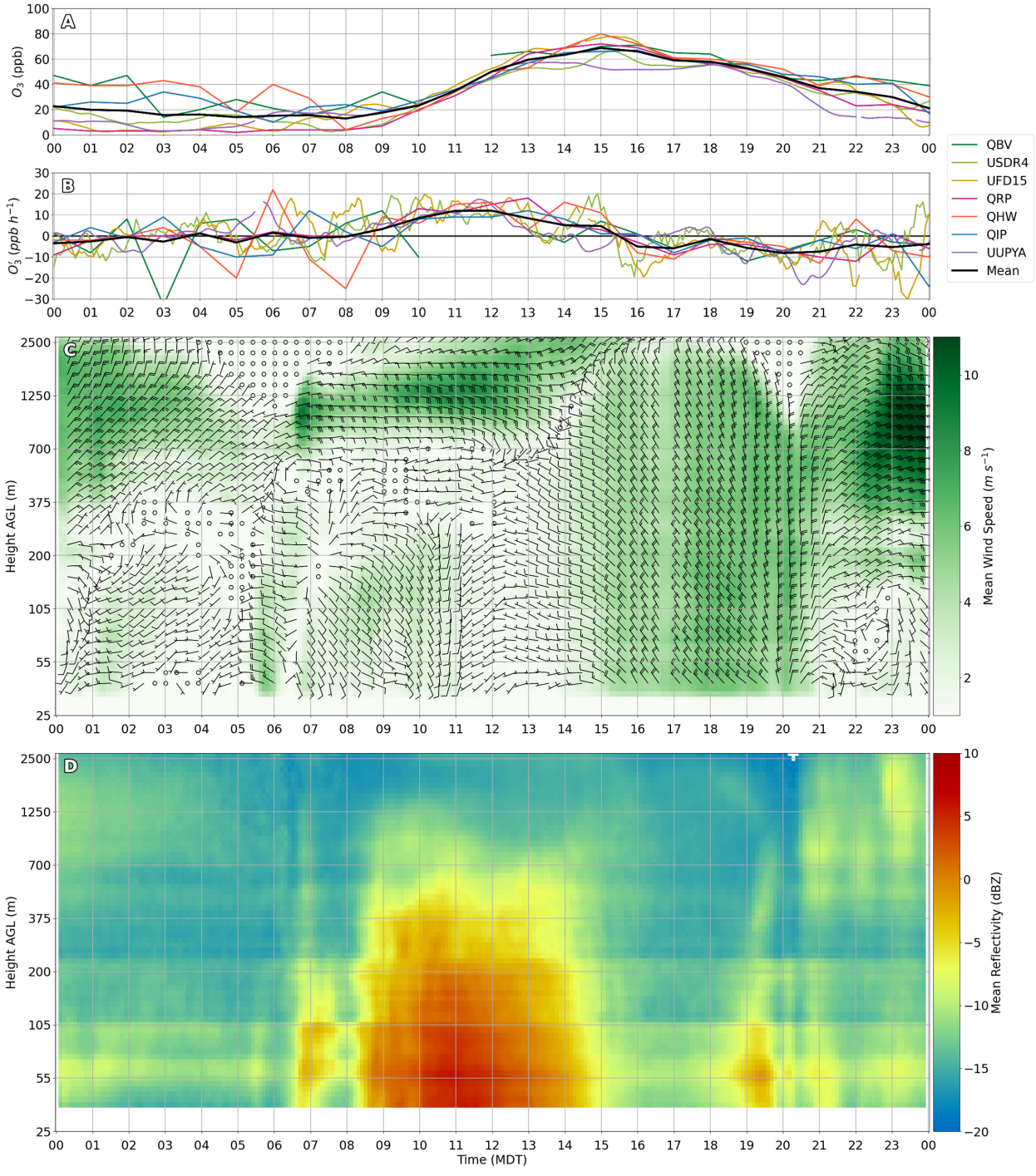

FIG. 6. Surface observations and radar retrievals 06 Sep 2022. (a) O_3 (ppb) from UDAQ and UU sites. (b) as in (a) except for O_3'. (c) TSLC VVP wind speed (fill) and subsampled wind barbs during 06 Sep 2022. Half (full) barbs correspond to 1.25 (2.5) $m\ s^{-1}$. Every second barb in time and third barb in height is shown. (d) TSLC mean reflectivity RD-QVP (dBZ) during 06 Sep 2022.

the nearby WSR-88D but is subjected to increased terrain blockage. The VVP and RD-QVP retrievals using a 5 km radius were used to observe the boundary layer during a high ozone period. Retrieval disks were partitioned along

a logarithmic height axis to enhance near-surface resolution. Limitations of retrieval accuracy with this geometry were assessed using artificial wind fields, which found that retrievals remained highly accurate, even when using noisy data.

Tropospheric ozone is a significant environmental hazard regulated by the EPA. The northern Wasatch Front is presently in moderate non-attainment of the $\overline{O_3}$ standard and have a complex set of thermally driven circulations from nearby mountains and the Great Salt Lake influencing observed concentrations. VVP and RD-QVP retrievals during an unusually high ozone period were calculated from TSLC and provided an unprecedented view of these processes. Shear layers frequently developed near the surface briefly after sunrise and increased in height throughout the day, yielding uniform flow through the depth of the profile in the afternoon. A reversal from off-shore to on-shore flows is present in the morning, likely corresponding to reversal of local thermally driven circulations. Profiles of individual days revealed flow interactions with the terrain that may have contributed to subtle differences in peak ozone concentrations. The shear layer matched reflectivity-derived boundary layer height estimates, which saw peak reflectivity near the time of flow reversal. The estimates diverged in the afternoon as deep turbulent mixing dispersed scatterers within the CBL, decreasing reflectivity.

TSLC has been used in this and prior studies to provide a more complete view of air-quality relevant boundary layer processes. Many other cities throughout the Intermountain West are also in non-attainment of EPA standards and are similarly influenced by flows in complex terrain. TDWRs located in Phoenix, Las Vegas, and Denver may provide further insights into local terrain's influence upon air quality by applying these retrieval methods. Utility of retrievals from TDWR may be limited in the winter months because of a lack of scatterers, in which case the differential reflectivity QVP method outlined in Banghoff et al. (2018) may be a better choice. However, WSR-88D radars in the west offering this product may struggle to capture key details due to high altitude siting locations and shallow clear-air coverage patterns.

Acknowledgments. The authors would like to thank Alex Jacques for assistance with processing surface meteorological and ozone data during the summer ozone project. We would also like to thank Colin Johnson for maintaining field study equipment and creating the figure outlining key sites. This work was possible due to the computing resources provided by the University of Utah's Center for High Performance Computing. The Python ARM Radar Toolkit (`Py_ART`) library was used extensively for radar data processing. Funding for this project was provided by the Utah Division of Air Quality and the NOAA/National Weather Service Collaborative Science, Technology, and Applied Research (CSTAR) Program, Award NA20NWS468046.

Data availability statement. Radar data used in this study are available from cloud providers as part of the NOAA Open Data Dissemination program.

References

Bachmann, S., and D. Zrnić, 2007: Spectral density of polarimetric variables separating biological scatterers in the VAD display. *J. Atmos. Oceanic Technol.*, **24 (7)**, 1186–1198, https://doi.org/10.1175/JTECH2043.1.

Baier, B. C., W. H. Brune, B. L. Lefer, D. O. Miller, and D. K. Martins, 2015: Direct ozone production rate measurements and their use in assessing ozone source and receptor regions for Houston in 2013. *Atmospheric Environment*, **114**, 83–91, https://doi.org/https://doi.org/10.1016/j.atmosenv.2015.05.033.

Banghoff, J. R., D. J. Stensrud, and M. R. Kumjian, 2018: Convective boundary layer depth estimation from S-Band dual-polarization radar. *J. Atmos. Oceanic Technol.*, **35 (8)**, 1723–1733, https://doi.org/10.1175/JTECH-D-17-0210.1.

Banta, R. M., and Coauthors, 2011: Dependence of daily peak O_3 concentrations near Houston, Texas on environmental factors: Wind speed, temperature, and boundary-layer depth. *Atmos. Environ.*, **45 (1)**, 162–173, https://doi.org/10.1016/j.atmosenv.2010.09.030.

Banta, R. M., and Coauthors, 2020: Characterizing NWP model errors using Doppler-lidar measurements of recurrent regional diurnal flows: Marine-air intrusions into the Columbia River Basin. *Mon. Wea. Rev.*, **148 (3)**, 929–953, https://doi.org/10.1175/MWR-D-19-0188.1.

Blaylock, B. K., J. D. Horel, and E. T. Crosman, 2017: Impact of lake breezes on summer ozone concentrations in the Salt Lake Valley. *J. Appl. Meteor. Climatol.*, **56 (2)**, 353–370, https://doi.org/10.1175/JAMC-D-16-0216.1.

Boccippio, D. J., 1995: A diagnostic analysis of the VVP single-doppler retrieval technique. *J. Atmos. Oceanic Technol.*, **12 (2)**, 230–248, https://doi.org/10.1175/1520-0426(1995)012⟨0230:ADAOTV⟩2.0.CO;2.

Brodin, M., D. Helmig, and S. Oltmans, 2010: Seasonal ozone behavior along an elevation gradient in the Colorado Front Range Mountains. *Atmos. Environ.*, **44 (39)**, 5305–5315, https://doi.org/10.1016/j.atmosenv.2010.06.033.

Browning, K. A., and R. Wexler, 1968: The determination of kinematic properties of a wind field using Doppler radar. *J. Appl. Meteor. Climatol.*, **7 (1)**, 105–113, https://doi.org/10.1175/1520-0450(1968)007⟨0105:TDOKPO⟩2.0.CO;2.

Cho, J. Y. N., 2005: Multi-PRI signal processing for the Terminal Doppler Weather Radar. Part II: Range–velocity ambiguity mitigation. *J. Atmos. Oceanic Technol.*, **22 (10)**, 1507–1519, https://doi.org/10.1175/JTECH1805.1.

Cho, J. Y. N., 2010: Signal processing algorithms for the Terminal Doppler Weather Radar: Build 2. Tech. Rep. ATC-363, MIT Lincoln Laboratory. 89 pp.

Chow, F. K., S. F. De Wekker, and B. J. Snyder, Eds., 2013: *Mountain Weather Research and Forecasting: Recent Progress and Current Challenges*, 261–289. Springer Netherlands, Dordrecht, https://doi.org/10.1007/978-94-007-4098-3_5, URL https://doi.org/10.1007/978-94-007-4098-3_5.

Chrust, M. F., C. D. Whiteman, and S. W. Hoch, 2013: Observations of thermally driven wind jets at the exit of Weber Canyon, Utah. *J. Appl. Meteor. Climatol.*, **52 (5)**, 1187–1200, https://doi.org/10.1175/JAMC-D-12-0221.1.

Clifton, O. E., and Coauthors, 2020: Dry deposition of ozone over land: Processes, measurement, and modeling. *Rev. Geophys.*, **58 (1)**, e2019RG000 670, https://doi.org/10.1029/2019RG000670.

Coates, J., K. A. Mar, N. Ojha, and T. M. Butler, 2016: The influence of temperature on ozone production under varying no_x conditions – a modelling study. *Atmospheric Chemistry and Physics*, **16 (18)**, 11 601–11 615, https://doi.org/10.5194/acp-16-11601-2016.

Crosman, E. T., and J. D. Horel, 2010: Sea and lake breezes: A review of numerical studies. *Boundary Layer Meteorol.*, **137 (1)**, 1–29, https://doi.org/10.1007/s10546-010-9517-9.

Crosman, E. T., and J. D. Horel, 2016: Winter lake breezes near the great salt lake. *Boundary Layer Meteorol.*, **159 (2)**, 439–464, https://doi.org/10.1007/s10546-015-0117-6.

Doviak, R. J., and D. S. Zrnic, 1993: *Doppler Weather Radar and Weather Observations*. 2nd ed., Dover Publications, Inc., 562 pp.

Fann, N., A. D. Lamson, S. C. Anenberg, K. Wesson, D. Risley, and B. J. Hubbell, 2012: Estimating the national public health burden associated with exposure to ambient pm2.5 and ozone. *Risk Analysis*, **32 (1)**, 81–95, https://doi.org/https://doi.org/10.1111/j.1539-6924.2011.01630.x.

Fast, J. D., and L. S. Darby, 2004: An evaluation of mesoscale model predictions of down-valley and canyon flows and their consequences using doppler lidar measurements during vtmx 2000. *Journal of Applied Meteorology*, **43 (3)**, 420 – 436, https://doi.org/https://doi.org/10.1175/1520-0450(2004)043⟨0420:AEOMMP⟩2.0.CO;2.

Goldberg, D. L., C. P. Loughner, M. Tzortziou, J. W. Stehr, K. E. Pickering, L. T. Marufu, and R. R. Dickerson, 2014: Higher surface ozone concentrations over the Chesapeake Bay than over the adjacent land: Observations and models from the DISCOVER-AQ and CBODAQ campaigns. *Atmos. Environ.*, **84**, 9–19, https://doi.org/10.1016/j.atmosenv.2013.11.008.

Griffin, E. M., T. J. Schuur, and A. V. Ryzhkov, 2018: A polarimetric analysis of ice microphysical processes in snow, using quasi-vertical profiles. *J. Appl. Meteor. Climatol.*, **57 (1)**, 31 – 50, https://doi.org/10.1175/JAMC-D-17-0033.1.

Holleman, I., 2005: Quality control and verification of weather radar wind profiles. *J. Atmos. Oceanic Technol.*, **22 (10)**, 1541–1550, https://doi.org/10.1175/JTECH1781.1.

Horel, J., E. Crosman, A. Jacques, B. Blaylock, S. Arens, A. Long, J. Sohl, and R. Martin, 2016: Summer ozone concentrations in the vicinity of the great salt lake. *Atmospheric Science Letters*, **17 (9)**, 480–486, https://doi.org/10.1002/asl.680.

Hu, J., and A. Ryzhkov, 2022: Climatology of the vertical profiles of polarimetric radar variables and retrieved microphysical parameters in continental/tropical MCSs and landfalling hurricanes. *J. Geophys. Res.*, **127 (5)**, e2021JD035 498, https://doi.org/10.1029/2021jd035498.

Hubbell, B. J., A. Hallberg, D. R. McCubbin, and E. Post, 2005: Health-related benefits of attaining the 8-hr ozone standard. *Environmental Health Perspectives*, **113 (1)**, 73–82, https://doi.org/10.1289/ehp.7186.

Jaffe, D., 2011: Relationship between surface and free tropospheric ozone in the western u.s. *Environmental Science & Technology*, **45 (2)**, 432–438, https://doi.org/10.1021/es1028102.

Kaser, L., and Coauthors, 2017: The effect of entrainment through atmospheric boundary layer growth on observed and modeled surface ozone in the colorado front range. *Journal of Geophysical Research: Atmospheres*, **122 (11)**, 6075–6093, https://doi.org/https://doi.org/10.1002/2016JD026245.

Liu, S. C., and Coauthors, 1992: A study of the photochemistry and ozone budget during the Mauna Loa Observatory Photochemistry Experiment. *J. Geophys. Res. Atmos.*, **97 (D10)**, 10 463–10 471, https://doi.org/10.1029/91JD02298.

Logan, J. A., M. J. Prather, S. C. Wofsy, and M. B. McElroy, 1981: Tropospheric chemistry: A global perspective. *Journal of Geophysical Research: Oceans*, **86 (C8)**, 7210–7254, https://doi.org/https://doi.org/10.1029/JC086iC08p07210.

Massey, J. D., W. J. Steenburgh, S. W. Hoch, and D. D. Jensen, 2017: Simulated and observed surface energy fluxes and resulting playa breezes during the MATERHORN field campaigns. *J. Appl. Meteor. Climatol.*, **56 (4)**, 915–935, https://doi.org/10.1175/JAMC-D-16-0161.1.

McCutchan, A. C., 2023: Terminal Doppler Weather Radar boundary layer observations during a summer high ozone period in complex terrain. M.S. thesis, Department of Atmospheric Sciences, University of Utah.

Melnikov, V. M., R. J. Doviak, D. S. Zrnić, and D. J. Stensrud, 2011: Mapping bragg scatter with a polarimetric wsr-88d. *Journal of Atmospheric and Oceanic Technology*, **28 (10)**, 1273 – 1285, https://doi.org/https://doi.org/10.1175/JTECH-D-10-05048.1.

NOAA Information Technology, 2023: NOAA Open Data Dissemination Program. URL https://www.noaa.gov/information-technology/open-data-dissemination, Accessed 6 Sep 2023.

NOAA NCEI, 2023a: Next Generation Weather Radar (NEXRAD). URL https://www.ncei.noaa.gov/products/radar/next-generation-weather-radar, Accessed 6 Sep 2023.

NOAA NCEI, 2023b: Terminal Doppler Weather Radar (TDWR). URL https://www.ncei.noaa.gov/products/radar/terminal-doppler-weather-radar, Accessed 6 Sep 2023.

Pichugina, Y. L., and Coauthors, 2019: Spatial variability of winds and HRRR–NCEP model error statistics at three Doppler-lidar sites in the wind-energy generation region of the Columbia River Basin. *J. Appl. Meteor. Climatol.*, **58 (8)**, 1633–1656, https://doi.org/10.1175/JAMC-D-18-0244.1.

Pusede, S. E., A. L. Steiner, and R. C. Cohen, 2015: Temperature and recent trends in the chemistry of continental surface ozone. *Chemical Reviews*, **115 (10)**, 3898–3918, https://doi.org/10.1021/cr5006815.

Ryzhkov, A., P. Zhang, H. Reeves, M. Kumjian, T. Tschallener, S. Trömel, and C. Simmer, 2016: Quasi-vertical profiles—A new way to look at polarimetric radar data. *J. Atmos. Oceanic Technol.*, **33 (3)**, 551–562, https://doi.org/10.1175/JTECH-D-15-0020.1.

Seinfeld, J. H., and S. N. Pandis, 2016: *Atmospheric chemistry and physics: from air pollution to climate change*. 3rd ed., Wiley, New York.

Shenghui, Z., W. Ming, W. Lijun, Z. Chang, and Z. Mingxu, 2014: Sensitivity analysis of the VVP wind retrieval method for single-Doppler weather radars. *J. Atmos. Oceanic Technol.*, **31 (6)**, 1289–1300, https://doi.org/10.1175/JTECH-D-13-00190.1.

Simpson, W. R., and Coauthors, 2007: Halogens and their role in polar boundary-layer ozone depletion. *Atmospheric Chemistry and Physics*, **7 (16)**, 4375–4418, https://doi.org/10.5194/acp-7-4375-2007.

Sousa, S. I. V., M. C. M. Alvim-Ferraz, and F. G. Martins, 2013: Health effects of ozone focusing on childhood asthma: What is now known – a review from an epidemiological point of view. *Chemosphere*, **90 (7)**, 2051–2058, https://doi.org/10.1016/j.chemosphere.2012.10.063.

Stull, R. B., 1988: *An Introduction to Boundary Layer Meteorology*. Kluwer Academic Publishers.

Teschke, G., and V. Lehmann, 2017: Mean wind vector estimation using the velocity–azimuth display (VAD) method: An explicit algebraic solution. *Atmos. Meas. Tech.*, **10 (9)**, 3265–3271, https://doi.org/10.5194/amt-10-3265-2017.

Tobin, D. M., and M. R. Kumjian, 2017: Polarimetric radar and surface-based precipitation-type observations of ice pellet to freezing rain transitions. *Wea. Forecasting*, **32 (6)**, 2065–2082, https://doi.org/10.1175/WAF-D-17-0054.1.

Waldteufel, P., and H. Corbin, 1979: On the analysis of single-doppler radar data. *J. Appl. Meteor. Climatol.*, **18 (4)**, 532–542, https://doi.org/10.1175/1520-0450(1979)018⟨0532:OTAOSD⟩2.0.CO;2.

Wentworth, G. R., J. G. Murphy, and D. M. L. Sills, 2015: Impact of lake breezes on ozone and nitrogen oxides in the Greater Toronto Area. *Atmos. Environ.*, **109**, 52–60, https://doi.org/10.1016/j.atmosenv.2015.03.002.

Wildmann, N., E. Päschke, A. Roiger, and C. Mallaun, 2020: Towards improved turbulence estimation with Doppler wind lidar velocity-azimuth display (VAD) scans. *Atmos. Meas. Tech.*, **13 (8)**, 4141–4158, https://doi.org/10.5194/amt-13-4141-2020.

Zrnic, D., and A. Ryzhkov, 1998: Observations of insects and birds with a polarimetric radar. *IEEE Trans. Geosci. Remote Sens.*, **36 (2)**, 661–668, https://doi.org/10.1109/36.662746.

Zumpfe, D. E., and J. D. Horel, 2007: Lake-breeze fronts in the salt lake valley. *J. Appl. Meteor. Climatol.*, **46 (2)**, 196–211, https://doi.org/10.1175/JAM2449.1.